Realizing Distance-Selective Interactions in a Rydberg-Dressed Atom Array

Simon Hollerith,[1,2,*] Kritsana Srakaew,[1,2] David Wei,[1,2] Antonio Rubio-Abadal,[1,2,†] Daniel Adler,[1,2,3] Pascal Weckesser,[1,2] Andreas Kruckenhauser,[4,5] Valentin Walther,[6,7] Rick van Bijnen,[4,5] Jun Rui,[1,2,8] Christian Gross,[1,2,9] Immanuel Bloch,[1,2,3] and Johannes Zeiher[1,2]

[1]*Max-Planck-Institut für Quantenoptik, 85748 Garching, Germany*
[2]*Munich Center for Quantum Science and Technology (MCQST), 80799 Munich, Germany*
[3]*Fakultät für Physik, Ludwig-Maximilians-Universität München, 80799 München, Germany*
[4]*Institute for Quantum Optics and Quantum Information of the Austrian Academy of Sciencies, Innsbruck, Austria*
[5]*Center of Quantum Physics, University of Innsbruck, Innsbruck, Austria*
[6]*ITAMP, Harvard-Smithsonian Center for Astrophysics, Cambridge, Massachusetts 02138, USA*
[7]*Department of Physics, Harvard University, Cambridge, Massachusetts 02138, USA*
[8]*Hefei National Laboratory for Physical Sciences at Microscale, University of Science and Technology of China, Hefei, Anhui 230026, People's Republic of China*
[9]*Physikalisches Institut, Eberhard Karls Universität Tübingen, 72076 Tübingen, Germany*

(Received 20 October 2021; accepted 24 January 2022; published 14 March 2022)

Measurement-based quantum computing relies on the rapid creation of large-scale entanglement in a register of stable qubits. Atomic arrays are well suited to store quantum information, and entanglement can be created using highly-excited Rydberg states. Typically, isolating pairs during gate operation is difficult because Rydberg interactions feature long tails at large distances. Here, we engineer distance-selective interactions that are strongly peaked in distance through off-resonant laser coupling of molecular potentials between Rydberg atom pairs. Employing quantum gas microscopy, we verify the dressed interactions by observing correlated phase evolution using many-body Ramsey interferometry. We identify atom loss and coupling to continuum modes as a limitation of our present scheme and outline paths to mitigate these effects, paving the way towards the creation of large-scale entanglement.

DOI: 10.1103/PhysRevLett.128.113602

The one-way or measurement-based quantum computer [1] has been suggested as an alternative to usual gate-based digital quantum computers. Contrary to the latter approach, the entanglement required for a calculation is created up front by creating a highly entangled cluster state [2], and the subsequent circuit is imprinted through controlled local measurements and subsequent feedback. Realizing such a scheme requires a single massively parallel entangling operation, which relies on controllable interactions [3–5] between all neighboring qubits in the register. The neutral-atom quantum computing platform is naturally amenable to parallel gate operation, as demonstrated in one dimension using collisional gates [6] or Rydberg atoms [5,7]. The dipolar nature of Rydberg interactions provides the toolbox for angular interaction control [8,9]. However, their long-range character makes it challenging to isolate atom pairs at a fixed distance for gate operations. This holds true for Rydberg dressing schemes where interactions are optically admixed to the ground state [10]. Rydberg dressing has been demonstrated to create Bell pairs in optical tweezers [10], to engineer long-range interacting Ising Hamiltonians [11,12] or to study the competition between dressed interactions and motion in an optical lattice [13]. A variety of further theoretical proposals to realize spin models [14–16] or extended Hubbard models [17,18] rely on enhanced interaction control.

Here, we demonstrate novel Rydberg-dressed interactions by coupling to bound Rydberg atom pairs, so-called Rydberg macrodimers [19–22]. In contrast to the soft-core potentials generated in standard dressing schemes [9,10], the resulting interactions are strongly selective in distance [3], see Fig. 1(a). We verify the presence of the dressed interactions in our two-dimensional optical lattice using many-body Ramsey interferometry [9]. In agreement with our calculations, we observe the buildup of two-spin and three-spin correlations at the fixed chosen distance. Finally, we identify how off-resonant scattering and photodissociation into unbound continuum states affect our dressing scheme, and discuss methods to mitigate the associated decoherence effects.

Traditionally, experiments using Rydberg atoms operate at large interatomic distances where their interaction

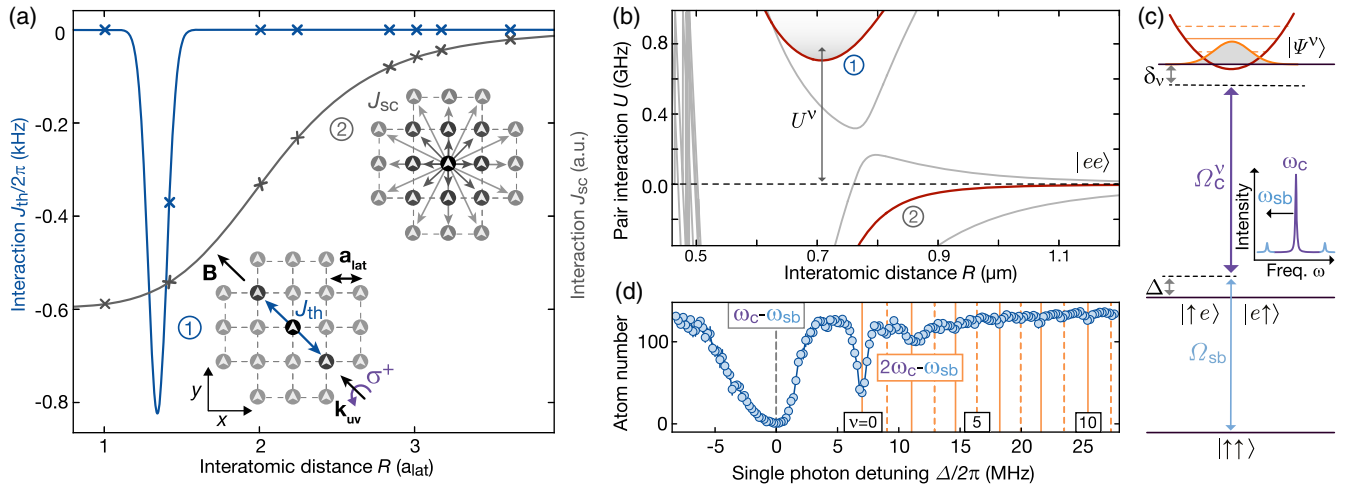

FIG. 1. Two-color Rydberg macrodimer dressing. (a) Utilizing macrodimer potentials for Rydberg dressing provides strongly localized interactions (blue), which are in stark contrast to typical soft-core interactions J_{sc} obtained by coupling to asymptotic interaction curves (gray). Crosses denote the distances present in the array. The spins are arranged in a two-dimensional square array with a spacing a_{lat} and are illuminated by the UV laser with wave vector $\mathbf{k}_{uv}$ oriented along the diagonal direction of the array and parallel to the magnetic field $\mathbf{B}$. At an interatomic distance $R = \sqrt{2}a_{lat}$ and an orientation $\mathbf{R}\|\mathbf{B}$, where the molecular Rabi couplings feature a narrow maximum, we expect to achieve a spin coupling $J_{th} = 2\pi \times 370(40)$ Hz. (b) At large distances, Rydberg interaction potentials are described by van der Waals interactions (gray marker). At smaller distances, one finds macrodimer binding potentials energetically shifted by U^ν from the asymptotic state $|ee\rangle$ (blue marker). (c) We perform a two-photon excitation scheme from the ground state $|\uparrow\uparrow\rangle$ via intermediate states $|\uparrow e\rangle$, $|e\uparrow\rangle$ detuned by Δ to molecular states $|\Psi^\nu\rangle$ using Rabi couplings Ω_{sb} and Ω_C^ν. In our dressing sequence, we work at finite two-photon detunings δ_ν to the molecular states. The two excitation fields are generated by modulating sidebands at frequencies $\omega_C \pm \omega_{sb}$ on our UV frequency ω_C. (d) Performing atom-loss spectroscopy, we find the vibrational spectrum slightly blue-detuned from the single-photon Rydberg transition coupled by the red sideband (here for $\omega_{sb} = 2\pi \times 723$ MHz).

potentials are well described by their asymptotic van der Waals character [23]. In the nonperturbative regime at closer distances and large interaction energies, crossings of pair potentials naturally occur. Avoided crossings then give rise to macrodimer binding potentials [22], see Fig. 1(b). Dressing to a vibrational series of these macrodimers leads to a fundamentally different interaction profile, which peaks at the distance matching the minimum of the binding potential, see Fig. 1(a). At the same time, long-distance tails are absent because the coupling to asymptotic pair potentials is negligibly small [3,24]. The width of the narrow interaction peaks is typically limited by the width of the ground state wave packet in the optical trap, which requires exquisite control over the motional states. Furthermore, the dressed interactions depend critically on the orientation of the molecular states relative to applied fields and light polarizations [25].

Our experiments started with a two-dimensional square atom array of about two hundred ^{87}Rb atoms in the electronic ground state $|\uparrow\rangle = |5S_{1/2}, F = 2, m_F = -2\rangle$ with a lattice spacing $a_{lat} = 532$ nm and a filling of 94(1)% [26]. The magnetic field $\mathbf{B}$ with absolute value $|\mathbf{B}| = 0.5$ G and the wave vector $\mathbf{k}_{uv}$ of the excitation laser at an ultraviolet (UV) wavelength $\lambda = 298$ nm were pointing along the lattice diagonal direction. The UV laser was σ^+ polarized along the magnetic field. The vibrational modes ν in the chosen macrodimer potential are energetically shifted by U^ν relative to the asymptotic pair state $|ee\rangle \equiv |36P_{1/2}36P_{1/2}\rangle$. We performed a two-photon and two-color excitation by modulating sidebands on our UV carrier frequency ω_C, see Fig. 1(c) [24]. The modulation frequency ω_{sb} was slightly below the interaction energy U^0 of the lowest vibrational state. Molecular states can then be excited by one sideband and one carrier photon, while other combinations remain off-resonant and do not contribute. Keeping ω_{sb} fixed and tuning the overall laser frequency, the vibrational modes are resonant at detunings $(\Delta/2\pi) = \frac{1}{2}[U^\nu - (\omega_{sb}/2\pi)]$ relative to the single-photon resonance between $|\uparrow\rangle$ and $|e\rangle$ driven by the red sideband, see Fig. 1(d). The observed suppression of excitation rates for higher vibrational modes is explained by increasing detunings Δ and smaller Franck-Condon integrals with the ground state wave packet. The two-color excitation scheme enables independent tunability of the intermediate-state detuning, the admixed scattering rates and the contributing light shifts [24]. Furthermore, it allowed us to strongly increase the coupling rates into the molecular states.

The molecular bond length $R_\nu = 712(5)$ nm $\approx \sqrt{2}a_{lat}$ restricts the coupling to molecular states oriented along the two lattice diagonals. For the chosen configuration of light

polarization and magnetic field, two-photon Rabi couplings Ω_ν between an atom pair $|\uparrow\uparrow\rangle$ into molecular states $|\Psi^\nu\rangle$ reach a strong maximum for $\mathbf{R}_\parallel = (+1,-1)a_{\mathrm{lat}}$ parallel to $\mathbf{B}$, while coupling rates at orthogonal orientation are suppressed [25]. This results in strong spin interactions $J_\parallel \equiv J$, while interactions $J_\perp \approx 0.06J$ along the orthogonal lattice diagonal direction are negligible on the timescale of our experiments. The interactions J arise at finite two-photon detunings δ_ν, where the molecular states are only virtually populated in a four-photon process [3] and the energy of a spin-up pair $|\uparrow\uparrow\rangle$ is reduced through $J \approx \sum_\nu \Omega_\nu^2/(4\delta_\nu)$ that was dominated by the lowest vibrational mode. Our single-photon Rabi frequency between $|\uparrow\rangle$ and $|e\rangle$ was calibrated to be $\Omega = 2\pi \times 2.83(5)$ MHz, our two-photon Rabi frequency is typically $\Omega_\nu \approx 2\pi \times 50$ kHz.

In a first experiment, we characterized the induced distance-selective interaction potential. To this end, we tuned our laser to a fixed intermediate-state detuning $\Delta/2\pi = 3.58$ MHz between the single-photon Rydberg resonance and the lowest vibrational resonance. The two-photon detunings are given by $\delta_\nu = \delta_0 - \nu\hbar\omega_\nu$ relative to the vibrational series. Here, δ_0 is the two-photon detuning relative to the lowest vibrational resonance $\nu = 0$. Furthermore, $\omega_\nu = 2\pi \times 3.80$ MHz is the vibrational spacing which is almost independent of ν because of the small anharmonicity of the binding potential. We realized a spin-1/2 system by including the hyperfine ground state $|\downarrow\rangle = |5S_{1/2}, F = 1, m_F = -1\rangle$, that was coupled to $|\uparrow\rangle$ by a microwave (MW) field but remained uncoupled to the molecular states. Neglecting irrelevant terms linear in the spin operators, the resulting spin lattice is thus described by the Ising Hamiltonian

$$\hat{H} = \hbar \sum_{i \neq j} \frac{J_{ij}}{2} \hat{S}_i^z \hat{S}_j^z, \tag{1}$$

where interactions $J_{ij} = J\delta_{i-j,\mathbf{R}_\parallel}$ are restricted to the coupled lattice diagonal and $\hat{S}_i^z(\hat{S}_j^z)$ are the z components of the spin operators at lattice sites $i(j)$. We studied the evolution of our atom array under Eq. (1) by performing Ramsey interferometry, see Fig. 2(a). After initializing all atoms in $|\uparrow\rangle$, a global $\pi/2$ pulse prepared the state $|\rightarrow\rangle^{\otimes N}$, with $|\rightarrow\rangle = (1/\sqrt{2})(|\downarrow\rangle - i|\uparrow\rangle)$ and N the total atom number in the system. Subsequently, we applied two UV dressing pulses with duration $t_{\mathrm{uv}}/2$, interrupted by a π rotation (spin echo) in order to cancel phases originating from single-atom shifts poportional to $\hat{S}_i^z$ [9]. During the evolution, coupled spin pairs accumulate phases $\varphi(t_{\mathrm{uv}}) = \pm J t_{\mathrm{uv}}$. We then closed the interferometer sequence using a final $\pi/2$ rotation, removed all atoms in the spin state $|\uparrow\rangle$ and measured the remaining atoms populating the state $|\downarrow\rangle$ using the single-site resolution of our quantum gas microscope [26]. In this projective measurement, we observe correlated spin flips using spatially averaged connected two-point correlators

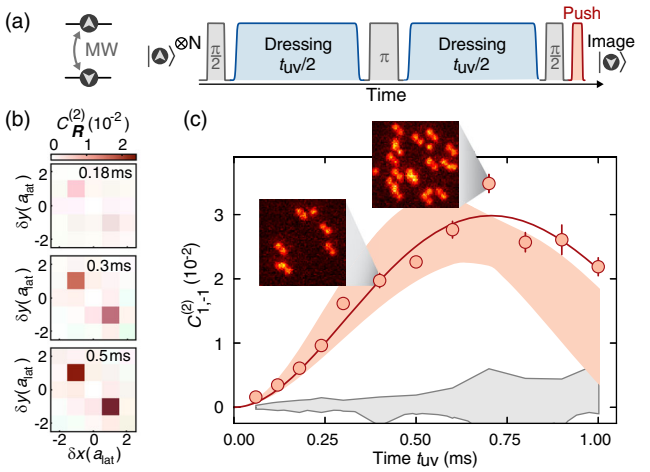

FIG. 2. Two-spin correlations. (a) We encode our spin states in two hyperfine ground states coupled by a microwave field. Spin interactions are probed using many-body Ramsey interferometry. (b) We evaluate spin-spin correlations $C^{(2)}_{\mathbf{R}}$ for increasing interaction time and find a strong signal at a distance $\mathbf{R} = (1,-1)a_{\mathrm{lat}}$ matching the strongly coupled lattice diagonal. The value at the origin was excluded. (c) The observed spin dynamics $C^{(2)}_{1,-1}(t)$ originates from correlated spin flips during the Ramsey sequence, as shown in exemplary images from our quantum gas microscope. Error bars in the correlation signal were calculated using a bootstrap algorithm (delete-1 jackknife). We fit the observed spin dynamics to a master equation and obtain $J = 2\pi \times 318(20)$ Hz and $\Gamma^{\mathrm{fit}}_{|\rightarrow\rangle} = 0.46(5)$ ms^{-1} (solid line). The red shaded area corresponds to the calculated dynamics using the same model with the calculated spin coupling J_{th} and the experimentally calibrated atom loss $\Gamma^{\mathrm{ex}}_{|\rightarrow\rangle} = 0.6(1)$ ms^{-1}. Here, uncertainties originate from J_{th} and $\Gamma^{\mathrm{ex}}_{|\rightarrow\rangle}$. The gray shaded region represents measured two-spin correlations $C^{(2)}_{\mathbf{R}}$ at other distances.

$C^{(2)}_{\mathbf{R}} = (\langle \hat{S}^z_{\mathbf{R}'} \hat{S}^z_{\mathbf{R}'+\mathbf{R}} \rangle - \langle \hat{S}^z_{\mathbf{R}'} \rangle \langle \hat{S}^z_{\mathbf{R}'+\mathbf{R}} \rangle)_{\mathbf{R}'}$, where $(.)_{\mathbf{R}'}$ denotes spatial averaging over all positions $\mathbf{R}'$ in the lattice. As expected for our selective interactions, we find that correlations are restricted to distances $\mathbf{R}_\parallel$, see Fig. 2(b). After an initial quadratic increase, correlations $C^{(2)}_{1,-1}(t)$ reach a maximum at $t_{\mathrm{uv}} = 0.7$ ms, which is consistent with a simulation assuming coherent spin dynamics. At later times t_{uv}, the signal is damped due to atom loss. Fitting a model including dissipation to the spin dynamics [27] yields a spin interaction of $J = 2\pi \times 318(20)$ Hz, close to the calculated value of $J_{\mathrm{th}} = 2\pi \times 370(40)$ Hz [see Fig. 2(c)].

A striking signature of our distance-selective spin interactions is the absence of a long-range tail. As a result, a coherent dephasing of the many-body dynamics can be avoided and one expects to observe revivals at $t_R = 2\pi/J$ in the bulk of the system. The realization of such a clean Ising Hamiltonian is particularly interesting because the coupled spins are expected to evolve into a highly entangled cluster state at times $t_C = t_R/2$ [6]. Although two-spin correlations

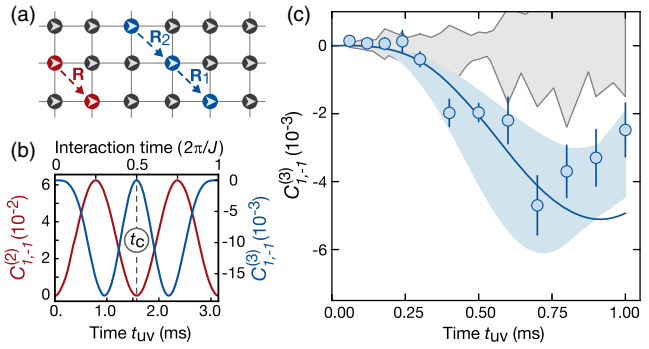

FIG. 3. Higher-order correlations. (a) In addition to $C^{(2)}_{1,-1}(t)$ (red), we expect to also observe connected three-spin correlations $C^{(3)}_{\mathbf{R_1R_2}}$ (blue) for distance vectors $\mathbf{R}_1 = \mathbf{R}_2 = (1,-1)a_{\mathrm{lat}}$ in our spin system. (b) A calculation for both correlators without dissipation reveals that $C^{(3)}_{1,-1}(t)$ is expected to appear with a delay relative to $C^{(2)}_{1,-1}(t)$. At a later time t_C, all coupled spins evolve into a cluster state. (c) Observed correlation dynamics of $C^{(3)}_{1,-1}(t)$. The solid line represents a calculation using the model parameters obtained by fitting $C^{(2)}_{1,-1}(t)$. The dynamics is in qualitative agreement with the calculation without dissipation but the amplitude of the signal is damped. The blue-shaded region represents the theoretical expectation. The gray shaded region represents the background at other distances $\mathbf{R_2}$ while $\mathbf{R_1} = (1,-1)a_{\mathrm{lat}}$. Error bars in the correlation signal are calculated using a bootstrap algorithm (delete-1 jackknife).

at uncoupled sites vanish [28], one expects the formation of multi-spin correlations. At t_C where $C^{(2)}_{1,-1}(t_C) = 0$, the system still features correlations on a global scale [29]. Here, we studied the emergence of higher-order correlations through the spatially averaged connected three-spin correlator $C^{(3)}_{\mathbf{R_1R_2}}$ [30]. We focus on $C^{(3)}_{1,-1}$ at distances $\mathbf{R_1} = \mathbf{R_2} = (1,-1)a_{\mathrm{lat}}$ where both pairs are coupled by J, as illustrated in Fig. 3(a). In a dissipationless system, a finite $C^{(3)}_{1,-1}$ value can be directly linked to three-partite entanglement [29]. Calculations in a bulk system at unity filling using the experimental value of J with vanishing dissipation are shown in Fig. 3(b), illustrating the revival dynamics of higher order correlations. In our spin system, we observe qualitatively similar dynamics, however, with a lower amplitude due to the presence of dissipation [see Fig. 3(c)]. We find that $C^{(3)}_{1,-1}(t)$ evolves with a delay compared to $C^{(2)}_{1,-1}(t)$, in agreement with our calculation. The buildup of multispin correlations by two-spin interactions can be understood because flipped spin pairs [11] constrain the dynamics of neighboring spins during the Hamiltonian dynamics.

At later times t_{uv}, atom loss becomes dominant, which limits us from observing coherent revival dynamics. From an independent experimental calibration, we extract the atom loss rate $\Gamma^{\mathrm{ex}}_{|\rightarrow\rangle} = 0.6(1)\ \mathrm{ms}^{-1}$, yielding a dressing quality factor of $J/\Gamma^{\mathrm{ex}}_{|\rightarrow\rangle} \approx 2\pi \times 0.5$ [30]. The observed value $\Gamma^{\mathrm{ex}}_{|\rightarrow\rangle}$ is above the calculated value $\Gamma^{\mathrm{th}}_{|\rightarrow\rangle} = 0.011\ \mathrm{ms}^{-1}$ assuming only off-resonant Rydberg and macrodimer scattering. This additional loss could be associated with off-resonant excitation by the near-resonant sideband, depended on the detuning Δ and the power in the sideband, and was independent of the macrodimer coupling. Possible origins include collective loss channels found in other Rydberg dressing experiments operating at high densities, potentially triggered by black-body radiation [9,31,32], as well as phase noise on the laser [33].

Besides atom loss, we identify a signature that is specific for macrodimers and their wave packets and limits dressing at low intermediate-state detunings. Our spectroscopy of the lowest vibrational resonance starting from $|\uparrow\rangle$ revealed a surprisingly strong ac-Stark shift V_{pd}, see Figs. 4(a) and 4(b). This originates from the coupling to a complete set of continuum modes for photodissociated states $|\uparrow e\rangle$, $|e\uparrow\rangle$, see Fig. 4(c). Summing over the contributing modes and accounting for their kinetic energies $E_k = \hbar\omega_k$ in the relative motion and bound-continuum Franck-Condon

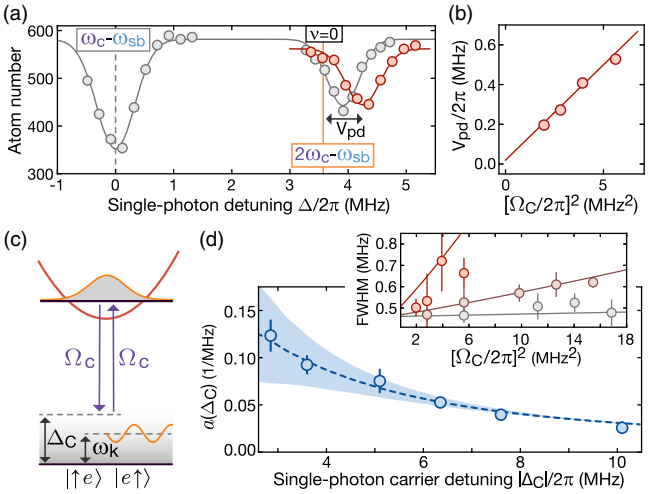

FIG. 4. Photodissociation into continuum modes. (a) Performing spectroscopy of the lowest vibrational line reveals a shift V_{pd} from the expected line position (orange), which increases with laser power (gray to red), here for $\omega_{\mathrm{sb}} = 2\pi \times 728$ MHz. (b) This linear light shift $V_{\mathrm{pd}}/(2\pi) = a(\Delta_C)[\Omega_C/(2\pi)]^2$ agrees very well with the theoretical model (solid line). (c) The calculation assumes a coupling Ω_C into singly excited pair states occupying motional continuum states by the carrier field. (d) By varying ω_{sb}, we measure the dependency of $a(\Delta_C)$ on the carrier detuning Δ_C between the molecular state and the intermediate state and find agreement with the calculation (dashed blue line). The blue shaded region indicates the varying contributions from different partial waves, which contribute to a broadening of the resonance, as shown in the inset for $\Delta_C/2\pi = -3.6, -6.35$, and -10.1 MHz (red to gray). Here, solid lines represent the theoretical expectation and error bars on the data points indicate the $1\sigma - 67\%$ confidence interval of fitted resonance profiles.

factors [34], we can predict the observed shift V_{pd}, see Figs. 4(b) and 4(d). The shift increases for smaller carrier detunings $\Delta_C = \delta_0 - \Delta$ and adds an offset to the detunings used in the calculation of the spin coupling. The coupling into the continuum furthermore broadens our resonance profiles, which will introduce dephasing to the spin dynamics at larger times t_{uv}, see the inset of Fig. 4(d). We attribute this to the varying individual light shifts of the angular partial waves contributing to the oriented macrodimer as well as on-resonant photodissociation into continuum states for $\Delta_C = -\omega_k$ [30]. During our dressing experiment, we chose values $\Delta_C/2\pi = -6.3$ and $\omega_{\mathrm{sb}} = 2\pi \times 726$ MHz where the effect of the broadening is small.

In conclusion, we realized Rydberg-dressed interactions restricted to a controllable selectable distance using macrodimers. At present, atom loss prevents us from observing coherent revivals. We anticipate an improvement by 1 order of magnitude in the dressing quality factor at unity Franck-Condon overlap. This can be achieved using shallower binding potentials available at larger distances and principal quantum numbers [24]. Here, also motional states contribute less because the vibrational wave packets carry less kinetic energy. In this scenario, we expect a preparation fidelity of 20% for a cluster state in a system of 25 atoms. In a cryogenic environment where losses approach the single-particle limit, this fidelity increases to 95%. Further improvements include encoding the qubit in a clock state with larger Ramsey coherence time, increasing the power and reducing the noise on the UV laser, reducing the densities [9,11] or performing potential engineering [35]. Symmetrizing the spin couplings in the plane through magnetic field and polarization control promises the creation of large-scale two-dimensional cluster states.

We thank all contributors to the open-source programs "pair interaction" and "ARC." Furthermore, we thank David Stephen for valuable discussions and Simon Evered for contributions to the experiment. We acknowledge funding by the Max Planck Society (MPG) and from Deutsche Forschungsgemeinschaft (DFG, German Research Foundation) under Germany's Excellence Strategy—EXC-2111–390814868 and Project No. BL 574/15-1 within SPP 1929 (GiRyd). This project has received funding from the European Union's Horizon 2020 research and innovation programme under Grant Agreement No. 817482 (PASQuanS) and the European Research Council (ERC) No. 678580 (RyD-QMB). K. S. acknowledges funding through a stipend from the International Max Planck Research School (IMPRS) for Quantum Science and Technology and J. R. acknowledges funding from the Max Planck Harvard Research Center for Quantum Optics. V. W. acknowledges support by the NSF through a grant for the Institute for Theoretical, Atomic, Molecular, and Optical Physics at Harvard University and the Smithsonian Astrophysical Observatory.

*Simon.Hollerith@mpq.mpg.de
†Present address: ICFO—Institut de Ciencies Fotoniques, The Barcelona Institute of Science and Technology, 08860 Castelldefels (Barcelona), Spain.

[1] R. Raussendorf and H. J. Briegel, Phys. Rev. Lett. **86**, 5188 (2001).
[2] M. Mamaev, R. Blatt, J. Ye, and A. M. Rey, Phys. Rev. Lett. **122**, 160402 (2019).
[3] R. M. W. van Bijnen and T. Pohl, Phys. Rev. Lett. **114**, 243002 (2015).
[4] A. Periwal, E. S. Cooper, P. Kunkel, J. F. Wienand, E. J. Davis, and M. Schleier-Smith, Nature (London) **600**, 630 (2021).
[5] H. Wu, X.-Y. Lin, Z.-X. Ding, S.-B. Zhen, I. Lesanovsky, and W. Li, arXiv:2110.12694.
[6] O. Mandel, M. Greiner, A. Widera, T. Rom, T. W. Hänsch, and I. Bloch, Nature (London) **425**, 937 (2003).
[7] H. Levine, A. Keesling, G. Semeghini, A. Omran, T. T. Wang, S. Ebadi, H. Bernien, M. Greiner, V. Vuletić, H. Pichler, and M. D. Lukin, Phys. Rev. Lett. **123**, 170503 (2019).
[8] S. de Léséleuc, V. Lienhard, P. Scholl, D. Barredo, S. Weber, N. Lang, H. P. Büchler, T. Lahaye, and A. Browaeys, Science **365**, 775 (2019).
[9] J. Zeiher, R. van Bijnen, P. Schauß, S. Hild, J.-Y. Choi, T. Pohl, I. Bloch, and C. Gross, Nat. Phys. **12**, 1095 (2016).
[10] Y.-Y. Jau, A. M. Hankin, T. Keating, I. H. Deutsch, and G. W. Biedermann, Nat. Phys. **12**, 71 (2016).
[11] J. Zeiher, J.-Y. Choi, A. Rubio-Abadal, T. Pohl, R. van Bijnen, I. Bloch, and C. Gross, Phys. Rev. X **7**, 041063 (2017).
[12] V. Borish, O. Marković, J. A. Hines, S. V. Rajagopal, and M. Schleier-Smith, Phys. Rev. Lett. **124**, 063601 (2020).
[13] E. Guardado-Sanchez, B. M. Spar, P. Schauss, R. Belyansky, J. T. Young, P. Bienias, A. V. Gorshkov, T. Iadecola, and W. S. Bakr, Phys. Rev. X **11**, 021036 (2021).
[14] A. W. Glaetzle, M. Dalmonte, R. Nath, I. Rousochatzakis, R. Moessner, and P. Zoller, Phys. Rev. X **4**, 041037 (2014).
[15] A. W. Glaetzle, R. M. W. van Bijnen, P. Zoller, and W. Lechner, Nat. Commun. **8**, 15813 (2017).
[16] L. I. R. Gil, R. Mukherjee, E. M. Bridge, M. P. A. Jones, and T. Pohl, Phys. Rev. Lett. **112**, 103601 (2014).
[17] G. Pupillo, A. Micheli, M. Boninsegni, I. Lesanovsky, and P. Zoller, Phys. Rev. Lett. **104**, 223002 (2010).
[18] T. Rakovszky, P. Sala, R. Verresen, M. Knap, and F. Pollmann, Phys. Rev. B **101**, 125126 (2020).
[19] C. Boisseau, I. Simbotin, and R. Côté, Phys. Rev. Lett. **88**, 133004 (2002).
[20] K. R. Overstreet, A. Schwettmann, J. Tallant, D. Booth, and J. P. Shaffer, Nat. Phys. **5**, 581 (2009).
[21] H. Saßmannshausen and J. Deiglmayr, Phys. Rev. Lett. **117**, 083401 (2016).
[22] S. Hollerith, J. Zeiher, J. Rui, A. Rubio-Abadal, V. Walther, T. Pohl, D. M. Stamper-Kurn, I. Bloch, and C. Gross, Science **364**, 664 (2019).
[23] S. Weber, C. Tresp, H. Menke, A. Urvoy, O. Firstenberg, H. P. Büchler, and S. Hofferberth, J. Phys. B **50**, 133001 (2017).

[24] M. Barbier, S. Hollerith, and W. Hofstetter, Phys. Rev. A **104**, 053304 (2021).
[25] S. Hollerith, J. Rui, A. Rubio-Abadal, K. Srakaew, D. Wei, J. Zeiher, C. Gross, and I. Bloch, Phys. Rev. Research **3**, 013252 (2021).
[26] C. Weitenberg, M. Endres, J. F. Sherson, M. Cheneau, P. Schauß, T. Fukuhara, I. Bloch, and S. Kuhr, Nature (London) **471**, 319 (2011).
[27] J. R. Johansson, P. D. Nation, and F. Nori, Comput. Phys. Commun. **183**, 1760 (2012).
[28] P. Richerme, Z.-X. Gong, A. Lee, C. Senko, J. Smith, M. Foss-Feig, S. Michalakis, A. V. Gorshkov, and C. Monroe, Nature (London) **511**, 198 (2014).
[29] M. C. Tran, J. R. Garrison, Z.-X. Gong, and A. V. Gorshkov, Phys. Rev. A **96**, 052334 (2017).
[30] See Supplemental Material at http://link.aps.org/supplemental/10.1103/PhysRevLett.128.113602 for details on the experiment and the calculations of macrodimer couplings.
[31] E. A. Goldschmidt, T. Boulier, R. C. Brown, S. B. Koller, J. T. Young, A. V. Gorshkov, S. L. Rolston, and J. V. Porto, Phys. Rev. Lett. **116**, 113001 (2016).
[32] J. A. Aman, B. J. DeSalvo, F. B. Dunning, T. C. Killian, S. Yoshida, and J. Burgdörfer, Phys. Rev. A **93**, 043425 (2016).
[33] L. Festa, N. Lorenz, L.-M. Steinert, Z. Chen, P. Osterholz, R. Eberhard, and C. Gross, Phys. Rev. A **105**, 013109 (2022).
[34] M. Peper and J. Deiglmayr, Phys. Rev. A **102**, 062819 (2020).
[35] D. Petrosyan and K. Mølmer, Phys. Rev. Lett. **113**, 123003 (2014).